

A generalized- α method for integrating the filtered Navier-Stokes equations with a stabilized finite element method

Kenneth E. Jansen^{a,1} Christian H. Whiting^{a,2}
Gregory M. Hulbert^b

^a*Scientific Computation Research Center and the Department of Mechanical Engineering, Aeronautical Engineering & Mechanics, Rensselaer Polytechnic Institute, Troy, New York, 12180-3590*

^b*Computational Mechanics Laboratory, Mechanical Engineering and Applied Mechanics, 2250 G. G. Brown, University of Michigan, Ann Arbor, MI 48109-2125*

Abstract

A generalized- α method is developed and analyzed for linear, first-order systems. The method is then extended to the filtered Navier-Stokes equations within the context of a stabilized finite element method. The formulation is studied through the application to laminar flow past a circular cylinder and turbulent flow past a long, transverse groove. The method is formulated to obtain a second-order accurate family of time integrators whose high frequency amplification factor is the sole free parameter. Such an approach allows the replication of midpoint rule (zero damping), Gear's method (maximal damping), or anything in between.

1 Introduction

As computational power increases, fluid dynamics researchers have been giving more attention to unsteady flows. In particular, the simulation of turbulence places very strict demands on the computational method due to its need to integrate a broad variation of spatial and temporal scales for very long time periods. The high temporal frequencies (often marginally resolved) can lead to non-physical instabilities if they are not controlled by high frequency damping. These poorly resolved frequencies, if left undamped, can also lead to further stiffening of the linear algebraic

¹ Corresponding author, supported by AFOSR grant F49620-97-1-0043

² Supported by NASA LaRC grant NGT-1-52160

system and, in some cases, to breakdown of the iterative methods used in its solution. However, the effect of this damping on the resolved scales present in the system must also be monitored to ensure that the dynamics of the resolved scales are faithfully represented.

While several methods have been proposed for the integration of the Navier-Stokes equations in time, there has yet to emerge one method as a clear favorite. Several have shown great promise on one type of flow only to perform unsatisfactorily in another. For example, space-time finite element methods were proposed and analyzed by Shakib et al.[1,2] and expanded and used extensively by Tezduyar et al.[3–6]. Here, as the name implies, the weight and solution space are given a temporal dependence in addition to the usual spatial dependence. While these methods have yielded very accurate results, the cost has only been justifiable on problems with a moving domain such as free surface flows and/or deforming spatial domains that account for moving solid boundaries. In these cases, the additional cost of space-time methods is put to good use by providing a consistent tracking of the moving boundary.

In cases where the boundary is not moving, semi-discrete methods remain in favor [7]. Semi-discrete methods discretize only space with the finite element method, leaving a system of ordinary differential equations to be integrated in time. Part of the attraction to semi-discrete methods is their long history of use in computational solid dynamics. Many algorithms have been proposed, analyzed and even designed to provide particular behavior needed in particular conditions. Of particular interest is the behavior of these algorithms in situations where a broad range of temporal scales are present. In this case, the time step is often chosen such that certain frequencies are marginally resolved or perhaps even completely unresolved. Given the non-linearities present in most interesting engineering systems, it is of great importance to ensure that there is temporal damping for frequencies beyond the chosen resolution level. However, it is equally important that this damping not effect the frequencies within the chosen resolution level. This delicate balancing act has lead to a long series of improvements to semi-discrete methods for computational solid dynamics as chronicled by Chung and Hulbert [8]. In the same reference a new method was developed and analyzed, termed the generalized- α method. In this paper we extend this analysis to computational fluid dynamics (i.e. from a second order system to a first order system) and provide validation and large scale applications where we can assess its efficiency and accuracy.

The outline of the paper is as follows. In Section 2 we introduce the filtered Navier-Stokes equations which we discretize in space using a stabilized finite element method to obtain a nonlinear system of coupled ordinary differential equations. Since this is a rather complicated environment to be explaining (not to mention analyzing) a new semi-discrete method, in Section 3 we introduce and analyze a linear model problem for these equations to allow illustration of the generalized- α method for first order systems. In Section 4, the method is extended to the system of interest and then verified on a simple model problem. The method is then applied to a large scale turbulence simulation to demonstrate its efficiency. Finally, in Section 5 some conclusions are drawn.

2 The Finite Element Formulation

Consider the compressible Navier-Stokes equations (complete with continuity and total energy equations) written in filtered form after the application of a subgrid-scale model (see Moin et al.[9], Moin & Jimenéz [10], Germano et al.[11], or Jansen [12,13] for details).

$$\mathbf{U}_{,t} + \mathbf{F}_{i,i}^{\text{adv}} - \mathbf{F}_{i,i}^{\text{diff}} = \mathcal{S} \quad (1)$$

where

$$\mathbf{U} = \begin{pmatrix} U_1 \\ U_2 \\ U_3 \\ U_4 \\ U_5 \end{pmatrix} = \bar{\rho} \begin{pmatrix} 1 \\ \tilde{u}_1 \\ \tilde{u}_2 \\ \tilde{u}_3 \\ \tilde{e}_{\text{tot}} \end{pmatrix}, \quad \mathbf{F}_i^{\text{adv}} = \tilde{u}_i \mathbf{U} + \bar{p} \begin{pmatrix} 0 \\ \delta_{1i} \\ \delta_{2i} \\ \delta_{3i} \\ \tilde{u}_i \end{pmatrix}, \quad \mathbf{F}_i^{\text{diff}} = \begin{pmatrix} 0 \\ \tau_{1i} \\ \tau_{2i} \\ \tau_{3i} \\ \tau_{ij} \tilde{u}_j - q_i \end{pmatrix} \quad (2)$$

and

$$\tau_{ij} = 2(\mu + \mu_T)(S_{ij}(\tilde{\mathbf{u}}) - \frac{1}{3}S_{kk}(\tilde{\mathbf{u}})\delta_{ij}) \quad , \quad S_{ij}(\tilde{\mathbf{u}}) = \frac{\tilde{u}_{i,j} + \tilde{u}_{j,i}}{2} \quad (3)$$

$$q_i = -(\kappa + \kappa_T)\tilde{T}_{,i} \quad , \quad \kappa_T = c_p \frac{\mu_T}{Pr_T} \quad , \quad \tilde{e}_{\text{tot}} = \tilde{e} + \frac{\tilde{u}_i \tilde{u}_i}{2} \quad , \quad \tilde{e} = c_v \tilde{T} \quad (4)$$

Where we use the overbar to denote an unweighted filter and a tilde to denote a density weighted filter. The filtered variables are: the velocity \tilde{u}_i , the pressure \bar{p} , the density $\bar{\rho}$, the temperature \tilde{T} and the total energy \tilde{e}_{tot} . The constitutive laws relate the stress, τ_{ij} , to the deviatoric portion of the strain, $S_{ij}^d = S_{ij} - \frac{1}{3}S_{kk}\delta_{ij}$, through a molecular viscosity, μ , plus turbulent viscosity, μ_T . Similarly, the heat flux, q_i , is proportional to the gradient of temperature with the proportionality constant given by the addition of a molecular conductivity, κ , and a turbulent conductivity, κ_T which is assumed proportional to the turbulent viscosity as described above. While the formulation is not limited to an ideal gas, $\bar{p} = \bar{\rho}R\tilde{T}$, and constant specific heats at constant pressure, c_p , and at constant volume, c_v , that is the model used in the calculations shown in this paper. Furthermore, since all the calculations shown in this paper are at low Mach number where temperature variation is low we have also assumed a constant molecular viscosity and constant conductivity through a constant Prandtl number, though, this again is not a necessary simplification. Finally \mathcal{S} is a body force (or source) term.

For the specification of the methods that follow, it is helpful to define the quasi-linear operator (with respect to some yet to be determined variable vector \mathbf{Y}) related to (1) as

$$\mathcal{L} \equiv \mathbf{A}_0 \frac{\partial}{\partial t} + \mathbf{A}_i \frac{\partial}{\partial x_i} - \frac{\partial}{\partial x_i} (\mathbf{K}_{ij} \frac{\partial}{\partial x_j}) \quad (5)$$

which can be naturally decomposed into time, advective, and diffusive portions

$$\mathcal{L} = \mathcal{L}_t + \mathcal{L}_{\text{adv}} + \mathcal{L}_{\text{diff}}. \quad (6)$$

Here $\mathbf{A}_i = \mathbf{F}_{i,\mathbf{Y}}^{\text{adv}}$ is the i^{th} Euler Jacobian matrix, \mathbf{K}_{ij} is the diffusivity matrix, defined such that $\mathbf{K}_{ij}\mathbf{Y}_{,j} = \mathbf{F}_i^{\text{diff}}$, and $\mathbf{A}_0 = \mathbf{U}_{,\mathbf{Y}}$ is the change of variables metric. For a complete description of $\mathbf{A}_0, \mathbf{A}_i$ and \mathbf{K}_{ij} , the reader is referred to [14]. Using this, we can write (1) as simply $\mathcal{L}\mathbf{Y} = \mathcal{S}$.

To proceed with the finite element discretization of the Navier-Stokes equations (1), we must define our finite element approximation spaces. First, let $\bar{\Omega} \subset \mathbf{R}^N$ represent the closure of the physical spatial domain (i.e. $\Omega \cup \Gamma$ where Γ is the boundary) in N dimensions, only $N = 3$ is considered here. In addition, $H^1(\Omega)$ represents the usual Sobolev space of functions with square-integrable values and derivatives on Ω .

Next, Ω is discretized into n_{el} finite elements, Ω^e . With this, we can define the trial solution space for the semi-discrete formulations as

$$\mathcal{V}_h = \{\mathbf{v} | \mathbf{v}(\cdot, t) \in H^1(\Omega)^m, t \in [0, T], \mathbf{v}|_{x \in \Omega^e} \in P_k(\Omega^e)^m, \mathbf{v}(\cdot, t) = \mathbf{g} \text{ on } \Gamma_g\}, \quad (7)$$

and the weight function space

$$\mathcal{W}_h = \{\mathbf{w} | \mathbf{w}(\cdot, t) \in H^1(\Omega)^m, t \in [0, T], \mathbf{w}|_{x \in \Omega^e} \in P_k(\Omega^e)^m, \mathbf{w}(\cdot, t) = \mathbf{0} \text{ on } \Gamma_g\}, \quad (8)$$

where $P_k(\Omega^e)$, is the space of all polynomials defined on Ω^e , complete to order $k \geq 1$, and m is the number of degrees of freedom ($m = 5$).

To derive the weak form of (1), the entire equation is dotted from the left by a vector of weight functions, $\mathbf{W} \in \mathcal{W}_h$, and integrated over the spatial domain. Integration by parts is then performed to move the spatial derivatives onto the weight functions (reducing the continuity requirements). This process leads to the integral equation (often referred to as the weak form): find $\mathbf{Y} \in \mathcal{V}_h$ such that

$$\begin{aligned} 0 = & \int_{\Omega} (\mathbf{W} \cdot \mathbf{U}_{,t} - \mathbf{W}_{,i} \cdot \mathbf{F}_i^{\text{adv}} + \mathbf{W}_{,i} \cdot \mathbf{F}_i^{\text{diff}}) d\Omega - \int_{\Gamma} \mathbf{W} \cdot (-\mathbf{F}_i^{\text{adv}} + \mathbf{F}_i^{\text{diff}}) n_i d\Gamma \\ & + \sum_{e=1}^{n_{el}} \int_{\Omega^e} \mathcal{L}^T \mathbf{W} \cdot \boldsymbol{\tau} (\mathcal{L}\mathbf{Y} - \mathcal{S}) d\Omega \end{aligned} \quad (9)$$

The first line of (9) contains the Galerkin approximation (interior and boundary) and the second line contains the least-squares stabilization. SUPG stabilization is obtained by replacing \mathcal{L}^T by $\mathcal{L}_{\text{adv}}^T$. The stabilization matrix $\boldsymbol{\tau}$ is an important ingredient in these methods and is well documented in Shakib [15] and in Franca and Frey [16]. Note that we have chosen to find \mathbf{Y} instead of \mathbf{U} . As discussed in Hauke and Hughes [17], \mathbf{U} is often not the best choice of solution variables, particularly when the flow is nearly incompressible. For the calculations performed herein, the SUPG stabilized

method was applied with linearly interpolated pressure-primitive variables viz.

$$\mathbf{Y} = \left\{ \begin{array}{c} Y_1 \\ Y_2 \\ Y_3 \\ Y_4 \\ Y_5 \end{array} \right\} = \left\{ \begin{array}{c} \bar{p} \\ \tilde{u}_1 \\ \tilde{u}_2 \\ \tilde{u}_3 \\ \tilde{T} \end{array} \right\} \quad (10)$$

By inspecting (2)-(4) it is clear that all quantities appearing in (9) may be easily calculated from (10).

To develop a numerical method, the weight functions (\mathbf{W}), the solution variable (\mathbf{Y}), and its time derivative ($\mathbf{Y}_{,t}$) are expanded in terms of basis functions (typically piecewise polynomials; all calculations described herein were performed with linear basis). The integrals (9) are then evaluated using Gauss quadrature resulting in a system of non-linear ordinary differential equations which can be written as

$$\mathbf{M}\dot{\underline{\mathbf{Y}}} = \mathbf{N}(\underline{\mathbf{Y}}) \quad (11)$$

where the under bar is added to make clear that $\underline{\mathbf{Y}}$ is the vector of solution values at discrete points (spatially interpolated with the finite element basis functions) and $\dot{\underline{\mathbf{Y}}}$ are the time derivative values at the same points.

3 Analysis of Generalized- α Method

The system of non-linear ordinary differential equations described in (11) is a nonlinear system, making it unwieldy for analysis. If we consider a linearized version, however, significant analysis can be performed. As described in Hughes [18] the linearized version of (11) can be un-coupled into many single degree of freedom problems with the help of orthogonal eigenvectors resulting in the following model problem

$$\dot{y} = \lambda y \quad (12)$$

where λ is the eigenvalue associated with the chosen mode.

We proceed to introduce the generalized- α method for integrating (12) from t_n to t_{n+1} (i.e. $\Delta_t =$

$t_{n+1} - t_n$)

$$\begin{aligned}
\dot{y}_{n+\alpha_m} &= \lambda y_{n+\alpha_f} \\
y_{n+1} &= y_n + \Delta_t \dot{y}_n + \Delta_t \gamma (\dot{y}_{n+1} - \dot{y}_n) \\
\dot{y}_{n+\alpha_m} &= \dot{y}_n + \alpha_m (\dot{y}_{n+1} - \dot{y}_n) \\
y_{n+\alpha_f} &= y_n + \alpha_f (y_{n+1} - y_n)
\end{aligned} \tag{13}$$

where α_m, α_f and γ are, at this point, free parameters. These four equations can be combined to yield the following system,

$$\mathbf{a}\mathbf{y}_{n+1} = \mathbf{b}\mathbf{y}_n, \quad \text{or} \quad \mathbf{y}_{n+1} = \mathbf{c}\mathbf{y}_n \tag{14}$$

where the solution vector at t_n is given by $\mathbf{y}_n = \{y_n, \Delta_t \dot{y}_n\}^T$ (similarly for \mathbf{y}_{n+1}) and the amplification matrix $\mathbf{c} = \mathbf{a}^{-1}\mathbf{b}$ is

$$\mathbf{c} = \frac{1}{d} \begin{bmatrix} \alpha_m - (\alpha_f - 1)\gamma\Omega & \alpha_m - \gamma \\ \Omega & \alpha_m - 1 + \alpha_f\Omega(1 - \gamma) \end{bmatrix} \tag{15}$$

where $\Omega = \lambda\Delta_t$ and $d = \alpha_m - \alpha_f\gamma\Omega$. It is fairly straightforward (see Hughes [18]) to show that

$$y_{n+1} = \mathbf{trace}(\mathbf{c})y_n - \mathbf{det}(\mathbf{c})y_{n-1} \tag{16}$$

If we further substitute a Taylor series expansion of y_{n+1} and y_{n-1} about y_n in time we find that second order accuracy can be obtained so long as

$$\gamma = \frac{1}{2} + \alpha_m - \alpha_f \tag{17}$$

This is the same result found by Chung and Hulbert [8] for the second order system.

Stability can be assessed by looking at the eigenvalues of \mathbf{c} . To make our model problem reflective of both advective and diffusive phenomena requires that Ω be complex. We are interested in proving stability for the left half of the complex plain since we will assume positive diffusive coefficients in our fluid dynamics problems. Stability will be attained so long as the modulus of each eigenvalue is less than or equal to one. The expressions for the eigenvalues of (15) are too lengthy to express here. Instead we will illustrate the stability constraints on α_m and α_f through the limiting values of Ω .

First consider the case when the time step is taken to be very small. Regardless of the value of λ , Ω vanishes, and the eigenvalues of \mathbf{c} in this limit are

$$\lim_{\Delta_t \rightarrow 0} \xi = \left\{ 1 - \frac{1}{\alpha_m}, 1 \right\} \tag{18}$$

from which we may deduce that stability requires

$$\alpha_m \geq \frac{1}{2} \quad (19)$$

We next consider the limit of an infinite time step for any eigenvalue in the left complex half plane (i.e Ω tending to complex infinity). The eigenvalues of \mathbf{c} in this limit are

$$\lim_{\Delta_t \rightarrow \infty} \xi = \left\{ \frac{-1 + 2(\alpha_m - \alpha_f)}{1 + 2(\alpha_m - \alpha_f)}, 1 - \frac{1}{\alpha_f} \right\} \quad (20)$$

from which we may deduce that stability also requires

$$\alpha_m \geq \alpha_f \geq \frac{1}{2} \quad (21)$$

Again, this is the same result obtained by Chung and Hulbert [8] for the second order system. Since they had an additional eigenvalue (and an additional parameter in their method) they had a third constraint that is not present here.

While having two parameters free in the method has a certain appeal we recall that our goal was to find a method with strict control of high frequency damping. Therefore it is enlightening to express the two parameters α_m and α_f in terms of the spectral radius of an infinite time step or maximum absolute value of the eigenvalue as Δ_t tends to infinity, what Chung and Hulbert referred to as ρ_∞

$$\rho_\infty = \lim_{\Delta_t \rightarrow \infty} \max(\xi_1, \xi_2) \quad (22)$$

By requiring the ρ_∞ from each eigenvalue in (20) to take on the same value we can express α_m and α_f in terms of ρ_∞ , viz.

$$\alpha_m = \frac{1}{2} \left(\frac{3 - \rho_\infty}{1 + \rho_\infty} \right), \quad \alpha_f = \frac{1}{1 + \rho_\infty} \quad (23)$$

thereby defining a second-order accurate family of methods with a specified high frequency damping.

The importance of casting the parameters in this way is that one has precise control over the damping of frequencies that are high relative to the resolution level. If ρ_∞ is chosen to be zero the method is said to annihilate the highest frequency in one step (only for a linear problem). This method has the same spectral stability as Gear's two step backward difference method [19]. If ρ_∞ is chosen to be one then the highest frequency (as well as all other others) are preserved (in the linear problem). This method corresponds to the midpoint rule which is equivalent to the trapezoidal rule for linear problems.

For linear problems with all frequencies resolved, the midpoint rule has the very nice property of introducing no damping regardless of the time step. However, when the λ is purely imaginary (i.e. when the flow is convection dominated) while the modulus remains equal to one, the eigenvalue $\lim_{\Omega \rightarrow \infty} \xi_1 = -1$ which has the effect of causing the solution to switch sign on each step. Clearly

this behavior is unacceptable. In these cases it is important to have ρ_∞ strictly less than one so that high frequencies do not spoil long term integrations. The example of vortex shedding from a circular cylinder (presented below) will illustrate this effect.

The problem is made worse by non-linearities. In many cases of interest ρ_∞ must be reduced to be substantially less than one to obtain an acceptable solution. The particularly attractive feature of this method is that a whole family of time integrators can be tested with precise control of ρ_∞ . In this way, ρ_∞ may be increased or decreased according to the needs of the problem of interest. Examples are given in Section 5 and 6 to illustrate this process.

4 Generalized- α Method for the Navier-Stokes Equations

The primary difficulty in extending the work from the previous section to the full Navier-Stokes equations is the non-linearity that is introduced. Straightforward extension of (13) to (11) leads to a non-linear system of algebraic equations to be solved at each step. For ease of presentation we also drop the under bar from the vector of nodal time derivatives of the solution $\underline{\dot{\mathbf{Y}}} \rightarrow \dot{\mathbf{Y}}$ and the vector of nodal values of the solution $\underline{\mathbf{Y}} \rightarrow \mathbf{Y}$ viz.

$$\mathbf{G}(\dot{\mathbf{Y}}_{n+\alpha_m}, \mathbf{Y}_{n+\alpha_f}) = \mathbf{M}_{n+\alpha_m} \dot{\mathbf{Y}}_{n+\alpha_m} - \mathbf{N}(\mathbf{Y}_{n+\alpha_f}) = \mathbf{0} \quad (24)$$

$$\mathbf{Y}_{n+1} = \mathbf{Y}_n + \Delta t \dot{\mathbf{Y}}_n + \gamma \Delta t (\dot{\mathbf{Y}}_{n+1} - \dot{\mathbf{Y}}_n) \quad (25)$$

$$\dot{\mathbf{Y}}_{n+\alpha_m} = \dot{\mathbf{Y}}_n + \alpha_m (\dot{\mathbf{Y}}_{n+1} - \dot{\mathbf{Y}}_n) \quad (26)$$

$$\mathbf{Y}_{n+\alpha_f} = \mathbf{Y}_n + \alpha_f (\mathbf{Y}_{n+1} - \mathbf{Y}_n) \quad (27)$$

$$(28)$$

Here we have introduced \mathbf{G} to be the vector of nodal values of the non-linear residual. The non-linearities are best handled by introducing a predictor-multicorrector algorithm similar to those proposed by Brooks and Hughes [20]. By making a prediction of the solution and its time derivative at time t_{n+1} we start the algorithm. Since we will be making multiple corrections, we introduce a superscript (inside parentheses) to represent the iteration number. In this notation our predictor is given an iteration count of zero and is given by

$$\mathbf{Y}_{n+1}^{(0)} = \mathbf{Y}_n \quad (29)$$

$$\dot{\mathbf{Y}}_{n+1}^{(0)} = \frac{\gamma - 1}{\gamma} \dot{\mathbf{Y}}_n \quad (30)$$

where (29) predicts that the solution will be the same as it was at the previous time step and (30) is the time derivative at t_{n+1} that is consistent with (25) (i.e. the predictor that preserves second order accuracy). Other choices of predictor are possible but discussion is left until later for clarity.

After making the prediction, the algorithm enters a loop of multi-corrector passes with i initialized

to zero. The first operation within the loop is the calculation of solution at $t_{n+\alpha_f}$ and the time-derivative of the solution at $t_{n+\alpha_m}$

$$\mathbf{Y}_{n+\alpha_f}^{(i)} = \mathbf{Y}_n + \alpha_f (\mathbf{Y}_{n+1}^{(i)} - \mathbf{Y}_n) \quad (31)$$

$$\dot{\mathbf{Y}}_{n+\alpha_m}^{(i)} = \dot{\mathbf{Y}}_n + \alpha_m (\dot{\mathbf{Y}}_{n+1}^{(i)} - \dot{\mathbf{Y}}_n) \quad (32)$$

These quantities enable the evaluation of $\mathbf{G}^{(i)}(\dot{\mathbf{Y}}_{n+\alpha_m}^{(i)}, \mathbf{Y}_{n+\alpha_f}^{(i)})$ which, for small i can be expected to be far from its desired value of $\mathbf{0}$. To find an improvement to the current values of (31) and (32) we utilize a Newton's linearization of $\mathbf{G}^{(i)}$ with respect to our solution variable viz.

$$\mathbf{G}^{(i)}(\dot{\mathbf{Y}}_{n+\alpha_m}^{(i)}, \mathbf{Y}_{n+\alpha_f}^{(i)}) + \frac{\partial \mathbf{G}^{(i)}(\dot{\mathbf{Y}}_{n+\alpha_m}^{(i)}, \mathbf{Y}_{n+\alpha_f}^{(i)})}{\partial \mathbf{Y}_{n+\alpha_f}^{(i)}} \Delta \mathbf{Y}_{n+\alpha_f}^{(i)} = \mathbf{0} \quad (33)$$

The first term of (33) is simply the non-linear residual. The second is the tangent matrix which tells us the direction to increment our solution (the third term) to improve our current iterate. This yields a linear matrix problem to be solved for each corrector step

$$\mathbf{K}^{(i)} \Delta \mathbf{Y}_{n+\alpha_f}^{(i)} = -\mathbf{G}^{(i)} \quad (34)$$

where $\mathbf{K}^{(i)}$ is the tangent matrix. Once this system is solved for $\Delta \mathbf{Y}_{n+\alpha_f}^{(i)}$, the solution is updated

$$\mathbf{Y}_{n+\alpha_f}^{(i+1)} = \mathbf{Y}_{n+\alpha_f}^{(i)} + \Delta \mathbf{Y}_{n+\alpha_f}^{(i)} \quad (35)$$

$$\dot{\mathbf{Y}}_{n+\alpha_m}^{(i+1)} = \left(1 + \frac{\alpha_m}{\gamma}\right) \dot{\mathbf{Y}}_n + \frac{\alpha_m}{\gamma \Delta t \alpha_m} (\mathbf{Y}_{n+\alpha_f}^{(i+1)} - \mathbf{Y}_n) \quad (36)$$

and i is incremented. If $i < i_{\max}$ the algorithm returns to solve (33) thus initiating the next corrector pass. Otherwise, the solution at time step t_{n+1} is determined as follows

$$\mathbf{Y}_{n+1} = \mathbf{Y}_n + \frac{\mathbf{Y}_{n+\alpha_f}^{(i_{\max})} - \mathbf{Y}_n}{\alpha_f} \quad (37)$$

$$\dot{\mathbf{Y}}_{n+1} = \dot{\mathbf{Y}}_n + \frac{\dot{\mathbf{Y}}_{n+\alpha_m}^{(i_{\max})} - \dot{\mathbf{Y}}_n}{\alpha_m} \quad (38)$$

This completes the step from $t_n \rightarrow t_{n+1}$. If more time steps are required, n is incremented and the algorithm returns to the prediction phase for the next step (i.e. (31) and (32)).

We have glossed over a few important aspects of the algorithm in the interest of a compact presentation. We address these issues in the remarks that follow.

REMARKS

- (1) There are at least three other predictors of interest. In the base algorithm we described a **Same $\dot{\mathbf{Y}}$** predictor. This predictor is the most robust but does little to accelerate convergence within a given time step for unsteady flows since it presumes the flow to be steady. For the

same reason it is the best predictor when a steady flow is desired. However, in this case one should not choose ρ_∞ based on (17,23) but should instead set $\alpha_m = \alpha_f = \gamma = 1$ to obtain the first-order accurate Backward Euler Method. The three alternative predictors are given below.

(a) Zero $\dot{\mathbf{Y}}$

$$\dot{\mathbf{Y}}_{n+1}^{(0)} = \mathbf{0} \quad (39)$$

$$\mathbf{Y}_{n+1}^{(0)} = \mathbf{Y}_n + \Delta_t(1 - \gamma) + \dot{\mathbf{Y}}_n \quad (40)$$

(b) Same $\dot{\mathbf{Y}}$

$$\dot{\mathbf{Y}}_{n+1}^{(0)} = \dot{\mathbf{Y}}_n \quad (41)$$

$$\mathbf{Y}_{n+1}^{(0)} = \mathbf{Y}_n + \Delta_t \dot{\mathbf{Y}}_n \quad (42)$$

(c) Same $\Delta \mathbf{Y}_{n+1} = \Delta \mathbf{Y}_n = \mathbf{Y}_n - \mathbf{Y}_{n-1}$

$$\mathbf{Y}_{n+1}^{(0)} = \mathbf{Y}_n + (\mathbf{Y}_{n+1} - \mathbf{Y}_n) \quad (43)$$

$$\dot{\mathbf{Y}}_{n+1}^{(0)} = \frac{\mathbf{Y}_n - \mathbf{Y}_{n-1}}{\Delta_t \gamma} + \frac{\gamma - 1}{\gamma} \dot{\mathbf{Y}}_n \quad (44)$$

These alternative predictors have shown superiority on some problems. However, they have also led to instabilities in some problems. It seems that the non-linearity can sometimes make minor changes in the predicted values lead to wild excursions from the solution of (24). Of the three, the **Same** $\Delta \mathbf{Y}_{n+1}$ offered the most improvement, often allowing i_{\max} to be reduced by one relative to the **Same** \mathbf{Y} . The downside of this predictor is that it cannot be used to start the algorithm (\mathbf{Y}_{n-1} is not available). However, it is possible to start with one of the other three predictors and switch to this predictor after the first step. Furthermore, after some manipulation of the formulas it is possible to update $\mathbf{Y}_{n+\alpha_f}^{(0)}$ and $\dot{\mathbf{Y}}_{n+\alpha_m}^{(0)}$ in place making this predictor not require more memory than the others as might have been suggested by (43) and (44).

- (2) The implementation given in (24) uses a “consistent” mass matrix, $\mathbf{M}_{n+\alpha_m}$, evaluated at $n+\alpha_m$. For the sake of computational convenience we often evaluate this term at $n+\alpha_f$ thereby avoiding the evaluation of the variables, \mathbf{Y} at a second temporal point for each quadrature point. The results have, in all cases compared, been insensitive to this shortcut motivating the albeit slight computational savings. This finding may be more reflective of the very mild non-linearities present in the mass term when using a pressure primitive variable formulation (for incompressible flow \mathbf{M} is independent of \mathbf{Y} making the point mute). Other, more highly non-linear variables (such as entropy variables) may be more sensitive to the treatment of this term.
- (3) The tangent matrix $\mathbf{K}^{(i)}$ is very large and very expensive to compute if done in the most straightforward way. There are a number ways in which the storage and the cost can be reduced due to the fact that iterative methods are usually employed to find a solution to solve (34). In particular, GMRES methods which were first proposed by Saad and Schultz [21] perform very well in conjunction with stabilized finite element methods applied to a variety of fluid dynamics problems. Shakib et al.[2] demonstrated the efficiency of element-by-element

GMRES solution techniques. Johan et al.[22] proposed a matrix-free extension to this work. We currently employ both solvers. Furthermore, we have recently linked our code with the PETSc solver library to enable testing of sparse storage implementations of GMRES as well as other solvers and a variety of pre-conditioners. Publications of this work are forthcoming.

- (4) Shakib et al.[2], Johan et al.[22], and many others have pointed out the importance of freezing the coefficient matrices (\mathbf{A}_0 , \mathbf{A}_i , and \mathbf{K}_{ij}) when calculating the tangent. This situation remains the same in our experience. Further simplifications are also possible. Semi-implicit methods can be created by neglecting completely various terms in the tangent. “Explicit” methods can be created by neglecting all terms but the time derivative term. The quotes around explicit reflect that consistent treatment of the time-derivative terms will still result in matrix problem unless the resulting matrix is lumped. Thus far, we have only studied the performance of this algorithm under the frozen coefficient, fully implicit case. The other cases are left for future work.
- (5) An important step in the linearization process is determining the dependence of $\dot{\mathbf{Y}}_{n+\alpha_m}^{(i)}$ on $\mathbf{Y}_{n+\alpha_f}^{(i)}$. The dependence is apparent from (36). This expression is obtained by solving for $\dot{\mathbf{Y}}_{n+\alpha_m}^{(i+1)}$ in (25-27). Recall that these are only nodal solution and time derivative vectors making the tangent

$$\frac{\partial \dot{\mathbf{Y}}_{A;n+\alpha_m}^{(i)}}{\partial \mathbf{Y}_{B;n+\alpha_f}^{(i)}} = \frac{\alpha_m \delta_{AB}}{\gamma \Delta_t \alpha_f} \quad (45)$$

where A and B are global node numbers considered to be selected from 1 to the number of nodal points, and δ_{AB} is the Kronecker delta function which is one only when $A = B$ and is otherwise zero. By including this term we implicitly account for the dependence of the nodal values of the time derivative of the solution on the nodal values of the solution that is built into the generalized- α method.

- (6) We have also omitted the discussion of boundary conditions. After each prediction or correction it is important to confirm that the solution satisfies the boundary conditions.

5 Validation on flow past a circular cylinder

The first example will provide an application of the generalized- α method to the relatively well understood flow around a circular cylinder at a Reynolds number of 100 (based on the cylinder diameter and inflow velocity). We have simulated this flow with compressible and incompressible stabilized finite element codes. Here we have chosen to present the incompressible code results since they are much more sensitive to the choice of time integration parameters. This incompressible formulation is completely described in Whiting and Jansen [23], and the details will not be given here.

The problem geometry and boundary conditions are depicted in Figure 1. In addition to the boundary conditions shown, we have imposed zero x_3 velocity and no tangential traction on the two x_3 planes to simulate 2 – d conditions with our 3 – d code. A complete description of this problem

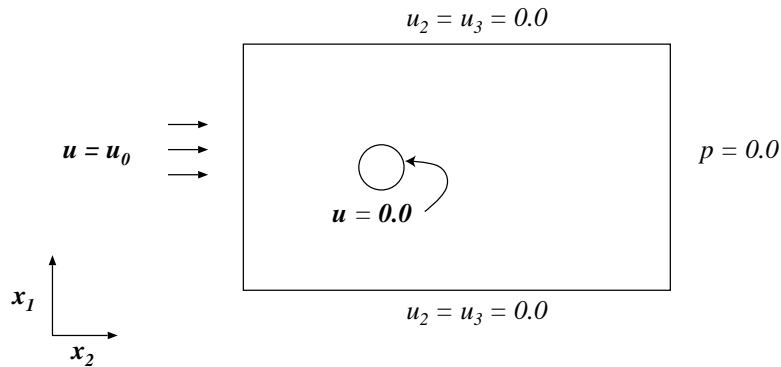


Fig. 1. Cylinder geometry and boundary conditions

can be found in variety of references: Shakib et al.[2], Hauke and Hughes [24], and Behr et al. [7]. We choose boundary conditions consistent with those of Shakib et al.[2]. At a Reynolds number of 100, the salient feature of this flow is the periodic shedding of vortices from the cylinder creating time varying lift and drag forces determined by integrating the forces on the cylinder surface. This single, dominant frequency allows a simple study of the new time integrator.

In this context, we will study the effect of the high-frequency damping parameter (ρ_∞) on the lift and drag profiles. The flow is solved in time assuming the cylinder is initially at rest, and is immediately accelerated to a velocity of \mathbf{u}_0 (often referred to as an impulsive start). We have taken a time step of 0.1 (normalized by the cylinder diameter) and for each time step, three Newton corrector passes are performed, insuring that the normalized change in the velocity increment is less than 5×10^{-4} . This time step affords 60 time steps per period of the lift force and 30 time steps per period of the drag force.

The first four plots in Figure 2 show the lift and drag forces (f_l and f_d , respectively) plotted against the non-dimensional time, t^* , for $\rho_\infty = 0.0, 0.25, 0.5,$ and 0.75 for two different time windows (the one on the right being a zoomed view). From these plots we make the following observations: *i*) the period and amplitude of both the lift and the drag are very weak functions of ρ_∞ (which might be expected from the observation that 30 points per wave length is adequate for second-order accurate methods), *ii*) a small amplitude undulation is present in the $\rho_\infty = 0.75$ case, *iii*) the elimination of this undulation for the cases of $\rho_\infty \leq 0.5$ reflects the increasing difficulty the method faces as ρ_∞ approaches 1, *iv*) the $\rho_\infty = 0$ case appears to start its transition from a steady separation to a saturated unsteady flow much earlier than the other methods.

The last observation is somewhat counter intuitive. One might expect the method with the highest damping would be the last to leave a steady flow in favor of an unsteady flow. The last two plots shed some light on this mystery. They indicate that the impulsive start can introduce a rather large, highest-frequency unsteadiness to the flow. Furthermore, these plots indicate the severe errors that may occur when using $\rho_\infty = 1.0$ (trapezoidal rule) for this flow. The first of these two plots shows the time window including the impulsive start. This plot clearly shows the strong damping characteristics of the $\rho_\infty = 0$ case, where the initial disturbance due to the impulsive start is damped out within a couple of time steps. Also clear from this plot is that the initial disturbance is almost completely preserved in the $\rho_\infty = 1$ case, polluting the entire solution. Intermediate

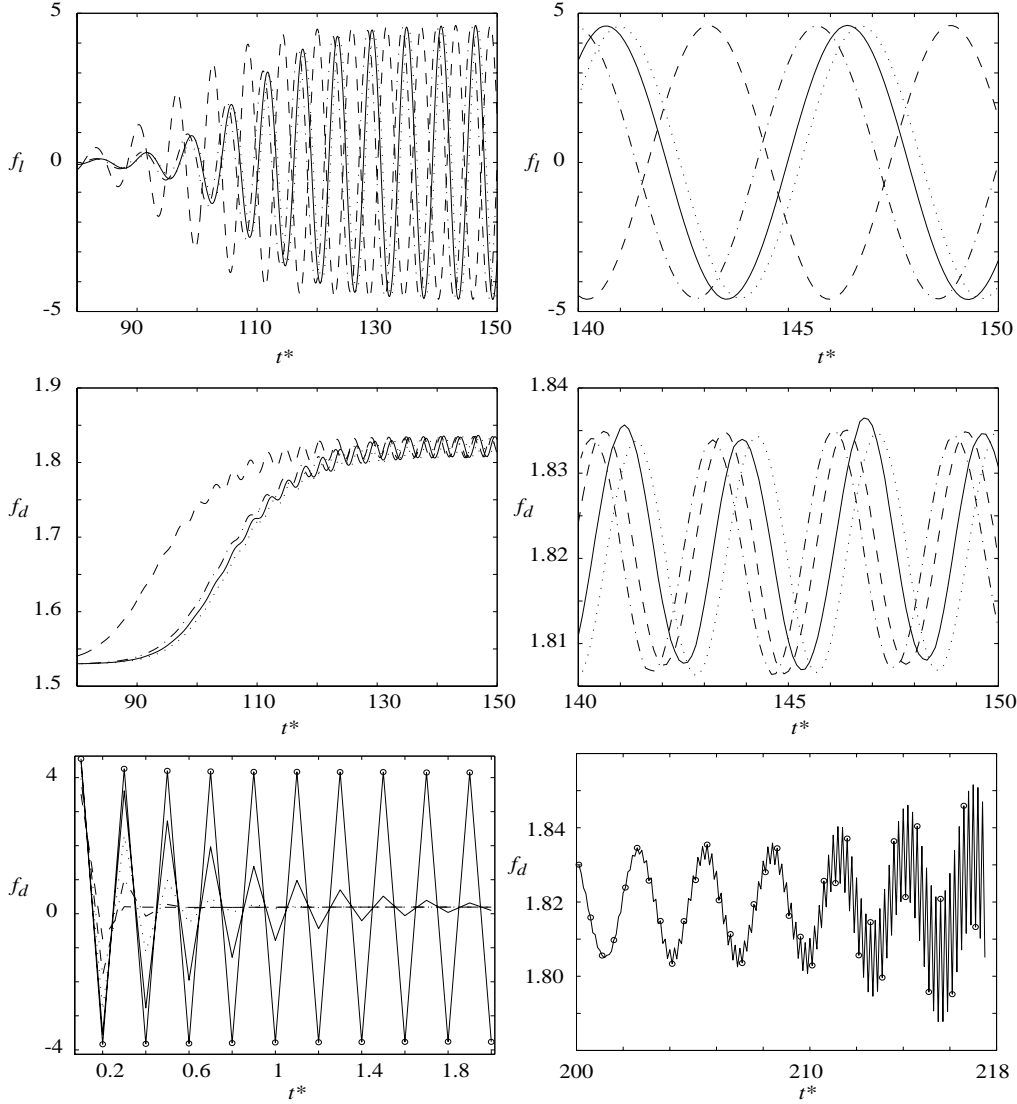


Fig. 2. Lift, f_l , and drag, f_d , forces on the cylinder for different time windows: — $\rho_\infty = 0.00$, --- $\rho_\infty = 0.25$, $\rho_\infty = 0.50$, - - - $\rho_\infty = 0.75$, and — \circ $\rho_\infty = 1.0$

values of ρ_∞ , annihilate this un-resolvable frequency in a manner predictable by their proximity to the two extreme cases. It is conjectured, that the physical instability leading to limit cycle vortex shedding is in the well resolved and almost completely undamped range for all chosen values of $0 \leq \rho_\infty \leq 1$. However, by using a shorter time to annihilate the highest, un-resolvable frequency, the lower values of ρ_∞ actually pick up the physical instability (which starts at extremely low values and grows exponentially before saturating on the limit cycle) sooner. The higher values of ρ_∞ are unable to pick up this very low amplitude physical instability until they bring the un-resolvable frequency below its level. This should not be misconstrued as an advocacy of $\rho_\infty = 0.0$ in all cases but it does demonstrate the benefit in at least one case of having the ability to annihilate

a large, un-resolvable frequency rapidly. In simulations of practical interest, this ability must be balanced by the fact that there often exist a continuous range of frequencies that one is interested in resolving rather than two, widely separated ones as shown here. In those cases, higher values of ρ_∞ are desirable to maintain the ability to accurately integrate waves with significantly less than 30-60 time steps per period.

The final plot in Figure 2 shows that the highest frequency can be excited even without an impulsive start. In this case the flow was restarted from case of $\rho_\infty = 0.0$ (at $t^* = 200$ where no high frequencies were visibly present). However, the nonlinearities inherent to the Navier-Stokes equations needed little time to build up energy in this highest frequency when the time integrator was switched to $\rho_\infty = 1.0$, a time integrator that is powerless to control these frequencies. This highest frequency mode does saturate in amplitude though leaving a surprisingly accurate signal that can be recovered by filtering this signal in time. This is again fortuitous to this case though, owing to the wide separation to the frequencies causing little if any interaction. Again it must be stressed that in the problems of interest, the continuous range of scales will suffer much greater contamination due to the stronger interaction of waves of close proximity in frequency space. In these cases the energy in the highest frequencies may also fail to saturate leading to a breakdown of the solution technique. Clearly, some capacity to insure the annihilation of un-resolvable waves is critical to maintain the fidelity of the well and marginally resolved waves, thus the motivation for the design of the method with careful control of ρ_∞ and the advocacy for the availability and use of intermediate values.

6 Application to turbulence simulation

The method described above has been applied to a number of turbulence simulations [13,12,25,26] including fundamental flows such as decay of isotropic turbulence and channel flow and very complex flows like a supersonic jet and flow over an airfoil. These simulations were large-eddy simulations (LES). As the name suggests, this turbulence simulation technique seeks to resolve the large eddies of the turbulent flow both in space and in time while modeling the turbulent eddies which fall below a certain cutoff of resolution. The need for high temporal accuracy with this technique was the driving motivation behind development of the method described above. In this section we will describe a recent application to flow over a very long cavity. A detailed study of this flow awaits results of ongoing calculations but results obtained thus far illustrate the fundamental character of the solutions obtained with this method.

6.1 Flow past a very long groove

Consider a turbulent boundary layer ($Re_\theta = U\theta/\nu = 1300$ where θ is the momentum thickness [27], and U is the speed of fluid in the free stream) encountering a very long groove, transverse to the flow direction. Since the groove is very long, the flow can be considered two-dimensional in the mean. Indeed, Reynolds-averaged Navier-Stokes simulations of this flow would be carried out using the two-dimensional geometry. However, to do the LES correctly requires resolution of the

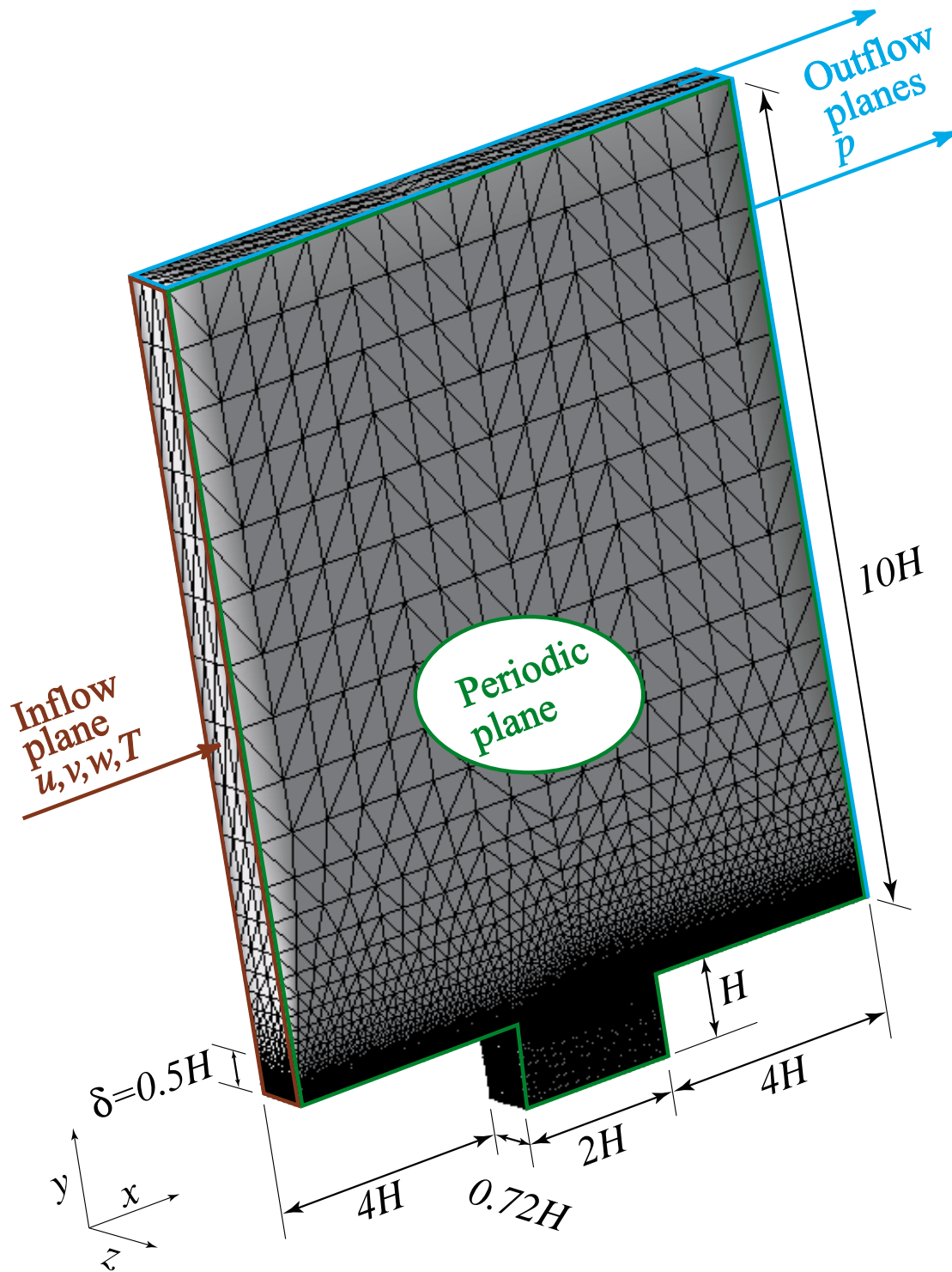


Fig. 3. Computational domain and boundary conditions. Outflow planes include the plane opposite the inflow and the top plane. Front periodic plane (shown) matches with back periodic plane (not shown). No slip, isothermal walls assumed (not shown) on plane, groove bottom, and two vertical groove walls.

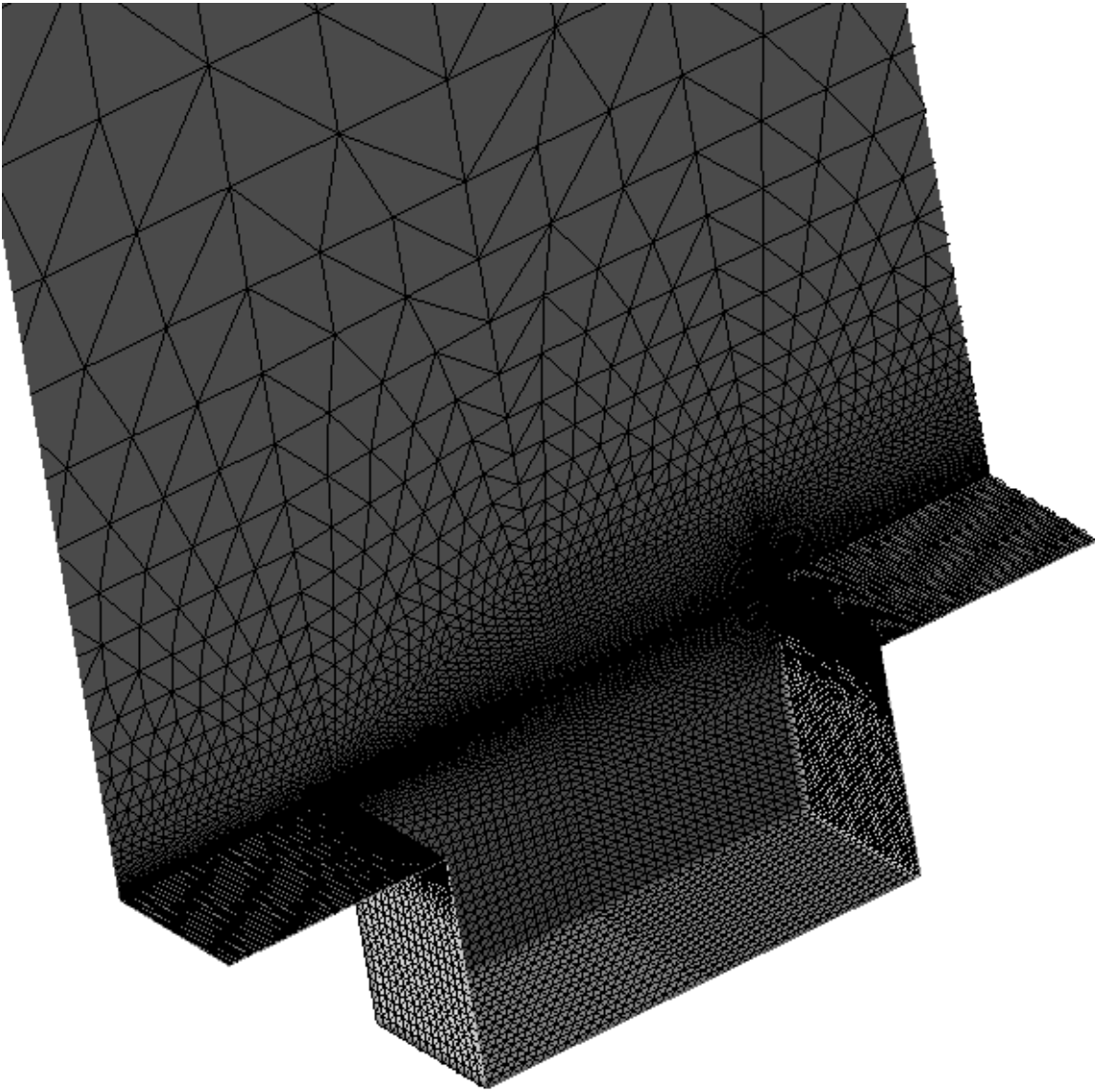


Fig. 4. Mesh on boundary with front plane, inflow plane and outflow plane cut away to show interior.

three-dimensional fluctuations. In this case, the simulation geometry is an extrusion of the two-dimensional cross-section of the groove into the transverse direction. The transverse length must be chosen long enough that the turbulent fluctuations are de-correlated (i.e. their two point correlation becomes very small) between the two lateral planes, the condition necessary for application of periodic boundary conditions.

Figure 3 illustrates the mesh on the boundary of the computational domain, with annotation of the physical dimensions and boundary conditions. The dimensions are normalized by the depth of the groove (H). From this we see that the groove length is twice the groove depth ($2H$) and that boundary layer thickness is about 50% of the groove depth ($0.5H$). A second Reynolds number is needed to characterize this problem, $Re_H = 27000$. As the groove height and length are varied, the fundamental character of the flow can be changed dramatically. In particular, for certain combinations, a resonance condition can occur wherein the fundamental frequency of the groove (and

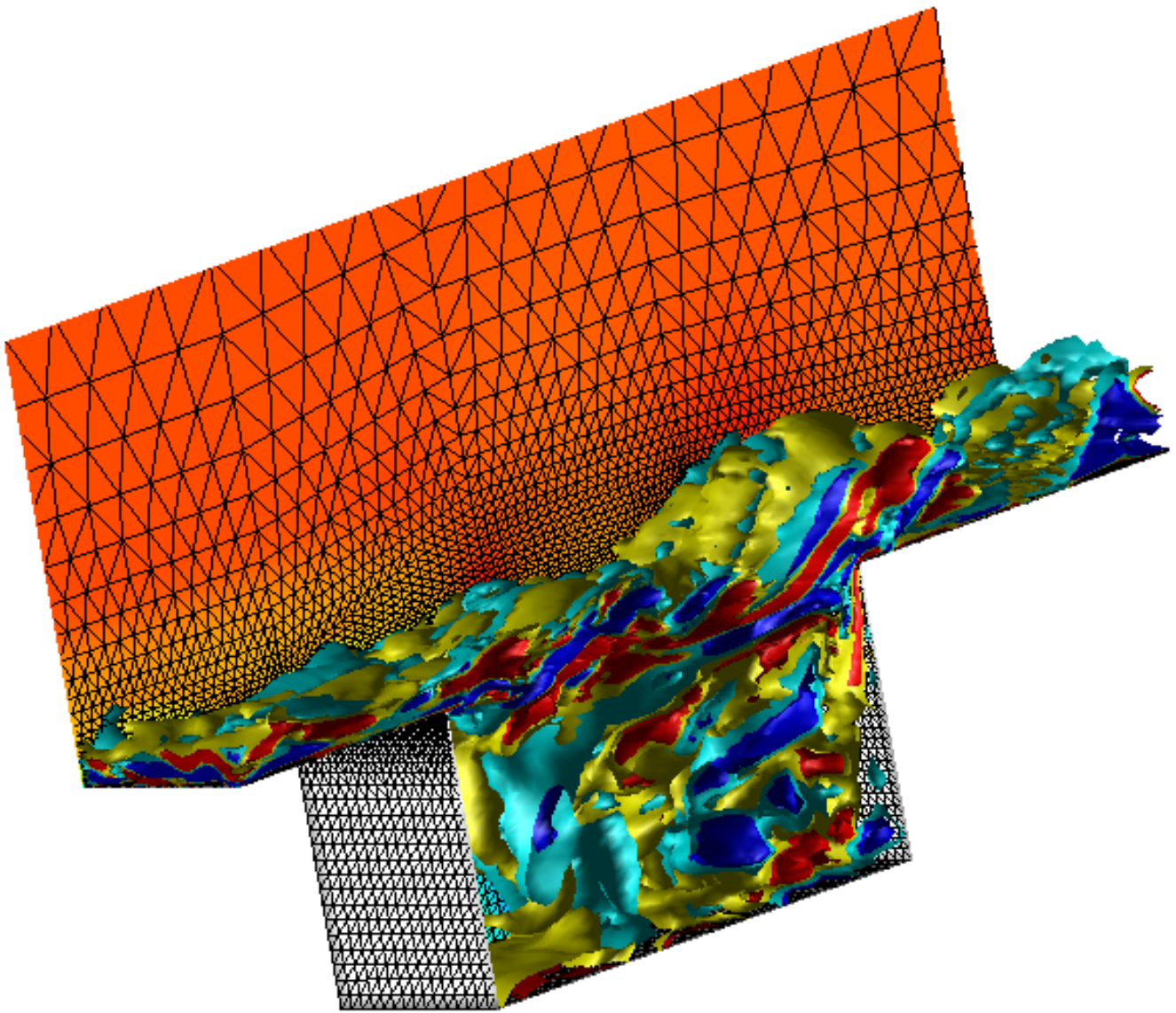


Fig. 5. Four isosurfaces of streamwise vorticity (red, large positive; dark blue, large negative value) with the streamwise velocity superposed on the back plane.

perhaps a few sub-harmonics) become quite strong (in contrast to the usual turbulence frequency spectrum which is rather broad and more equally distributed) turning an otherwise nearly silent device into a whistle. In some engineering devices, this phenomena is quite deleterious and therefore worthy of design effort to avoid.

Before showing solutions to this problem we turn our attention to Figure 4 where we have zoomed in on the groove relative to Figure 3 and removed the front and side walls to allow viewing of the grid resolution on all surfaces. Note in particular, the very fine near-wall resolution on the incoming turbulent boundary layer before the groove. This fine grid is necessary to resolve the turbulent eddies in the near wall region as shown in Figure 5 through isosurfaces of the streamwise vorticity. These small vortices which are created by the wall shear are freed from the wall at the groove inception creating a free shear layer. The growth of these structures is matched by a growth in the grid as can

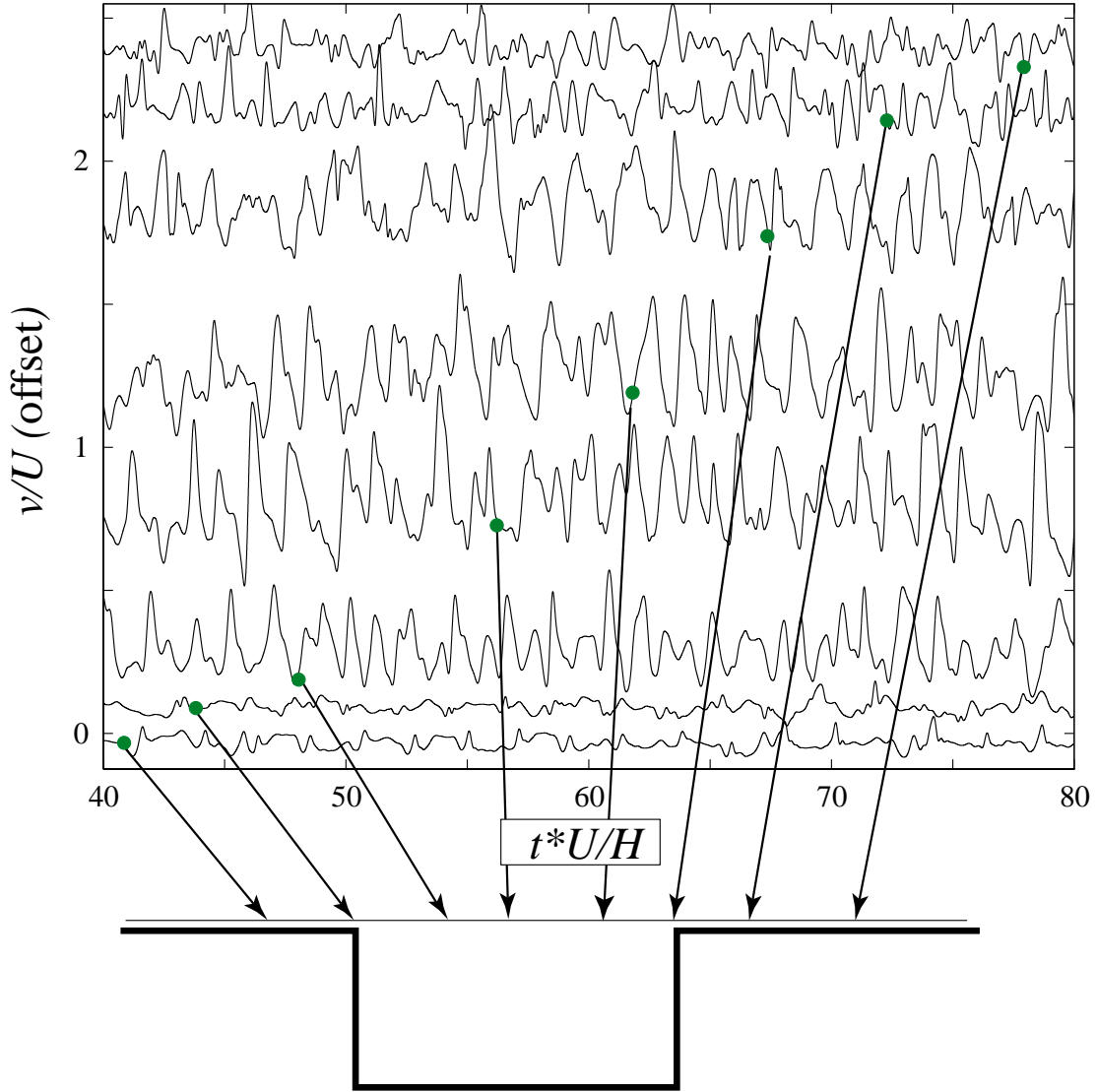


Fig. 6. Time series of vertical velocity collected at various positions at each time step.

be seen by referring back to Figure 4. This shear layer is unstable, causing the streamwise vortices to roll up in much the same way as in the laminar Kelvin-Helmholtz instability.

The free shear layer is again interrupted by the end of the groove, where it is seen to impact upon the groove far wall. At this point, the flow is divided, some going over the groove, some going down the far wall. This downward flow, combined with the shear across the top of the groove, causes a complicated driven “cavity” flow within the groove. The fluctuations from this cavity flow feed back to the very base of the shear layer at the groove inception.

This flow has a number of complex features that provide challenges for accurate simulation. As the primary topic of this paper is the description of a new time integrator we will confine our discussion to those related to temporal integration. The simulation was performed with $\rho_\infty = 0.5$ and a time step of $0.002H/U$ resulting in an average of 10 GMRES Krylov vectors per solve.

Simulations performed at a higher value of ρ_∞ required significantly more Krylov vectors (due to equation stiffening associated with un-resolvable high frequencies), and based on the cylinder results, additional damping was judged to be acceptable. The impinging flow on the vertical groove flow is most likely the source of the high frequencies in this flow, necessitating the reduction of ρ_∞ . Though the results are preliminary, Figure 6 shows the time history of the vertical velocity according to the LES solution at various points within the flow. One can see the changing character from a turbulent boundary layer (where vertical velocity fluctuations are suppressed by the solid wall) to a free shear layer (where the instabilities grow and appear to be locking onto the fundamental frequency) then, after the groove, the recovery back to a turbulent boundary layer. Clearly, simulations of this type require not only high spatial accuracy [28] but also, accurate, well understood, temporal accuracy.

7 Conclusions

A generalized- α method was developed and analyzed for linear, first-order systems. A key desirable attribute of the method is that it allows the high frequency amplification factor to be set directly, thereby developing a range of time integrators from zero damping midpoint rule to maximal damping Gear's method (or anything in between). The method was then extended to the filtered Navier-Stokes equations within the context of a stabilized finite element method. Two applications were given; one quite simple (laminar vortex shedding behind a circular cylinder), where the behavior of the high frequency damping factor could be observed, and another quite complex (turbulent flow over a very long transverse groove), where the need for such an integrator is made evident.

8 Acknowledgments

The authors also acknowledge Francois Bastin and Farzin Shakib whose early discussions aided the algorithmic development of the generalized- α method for the Navier-Stokes equations.

This work has been supported by the AFOSR (F49620-97-1-0043), by NASA LaRC (NGT-1-52160), and by the Center for Turbulence Research (CTR) (a joint NASA-Stanford University program). It has also enjoyed generous computer resources from the Army High Performance Computing Research Center (AHPCRC) and the Naval Research Lab (NRL).

References

- [1] F. Shakib and T. J. R. Hughes, "A new finite element formulation for computational fluid dynamics: IX. Fourier analysis of space-time Galerkin/least-squares algorithms", *Comp. Meth. Appl. Mech. Engng.*, **87** (1991) 35–58.

- [2] F. Shakib, T. J. R. Hughes, and Z. Johan, “A new finite element formulation for computational fluid dynamics: X. The compressible Euler and Navier-Stokes equations”, *Comp. Meth. Appl. Mech. Engng.*, **89** (1991) 141–219.
- [3] T. E. Tezduyar, M. Behr, and J. Liou, “New strategy for finite element computations involving moving boundaries and interfaces. The deforming-spatial-domain/space-time procedure. I. the concept and the preliminary numerical tests”, *Comp. Meth. Appl. Mech. Engng.*, **94** (1992) 339–351.
- [4] T. E. Tezduyar, M. Behr, and J. Liou, “New strategy for finite element computations involving moving boundaries and interfaces. The deforming-spatial-domain/space-time procedure. II. Computation of free-surface flows, two-liquid flows, and flows with drifting cylinders”, *Comp. Meth. Appl. Mech. Engng.*, **94** (1992) 339–351.
- [5] A. A. Johnson and T. E. Tezduyar, “Mesh update strategies in parallel finite element computations of flow problems with moving boundaries and interfaces”, *Comp. Meth. Appl. Mech. Engng.*, **119** (1994) 73–94.
- [6] A. A. Johnson and T. E. Tezduyar, “3D simulation of fluid-particle interactions with the number of particles reaching 100”, *Comp. Meth. Appl. Mech. Engng.*, **145** (1997) 301–321.
- [7] M. Behr, D. Hastreiter, S. Mittal, and T. E. Tezduyar, “Incompressible flow past a circular cylinder: dependence of the computed flow field on the location of the lateral boundaries”, *Comp. Meth. Appl. Mech. Engng.*, **123** (1996) 309–316.
- [8] J. Chung and G. M. Hulbert, “A time integration algorithm for structural dynamics with improved numerical dissipation: The generalized- α method”, *Journal of Applied Mechanics*, **60** (1993) 371–75.
- [9] P. Moin, K. Squires, W. H. Cabot, and S. Lee, “A dynamic subgrid-scale model for compressible turbulence and scalar transport”, *Physics of Fluids*, **3** (1991) 2746–2757.
- [10] P. Moin and J. Jimenéz, “Large-eddy simulation of complex turbulent flows”, in *AIAA 24th Fluid Dynamics Conference*. AIAA-93-3099, (1993).
- [11] M. Germano, U. Piomelli, P. Moin, and W. H. Cabot, “A dynamic subgrid-scale eddy viscosity model”, *Physics of Fluids*, **3** (1991) 1760.
- [12] K.E. Jansen, “Large-eddy simulation using unstructured grids”, in C. Liu and Z. Liu, editors, *Advances in DNS/LES*, Greyden Press, Columbus, Ohio, (1997) 117–128.
- [13] K. E. Jansen, “A stabilized finite element method for computing turbulence”, *Comp. Meth. Appl. Mech. Engng.*, (accepted for publication).
- [14] G. Hauke, *A unified approach to compressible and incompressible flows and a new entropy-consistent formulation of the $k-\epsilon$ model*, Ph.D. thesis, Stanford University, 1995.
- [15] F. Shakib, *Finite element analysis of the compressible Euler and Navier-Stokes equations*, Ph.D. thesis, Stanford University, 1989.
- [16] L. P. Franca and S. Frey, “Stabilized finite element methods: II. The incompressible Navier-Stokes equations”, *Comp. Meth. Appl. Mech. Engng.*, **99** (1992) 209–233.
- [17] G. Hauke and T. J. R. Hughes, “A unified approach to compressible and incompressible flows”, *Comp. Meth. Appl. Mech. Engng.*, **113** (1994) 389–396.

- [18] Thomas J. R. Hughes, *The finite element method: Linear static and dynamic finite element analysis*. Prentice Hall, Englewood Cliffs, NJ, 1987.
- [19] C.W. Gear, *Numerical initial value problems in ordinary differential equations*. Prentice-Hall, Englewood Cliffs, NJ, 1971.
- [20] A. N. Brooks and T. J. R. Hughes, “Streamline upwind / Petrov-Galerkin formulations for convection dominated flows with particular emphasis on the incompressible Navier-Stokes equations”, *Comp. Meth. Appl. Mech. Engng.*, **32** (1982) 199–259.
- [21] Y. Saad and M.H. Schultz, “GMRES: A generalized minimal residual algorithm for solving nonsymmetric linear systems”, *SIAM Journal of Scientific and Statistical Computing*, **7** (1986) 856–869.
- [22] Z. Johan, T. J. R. Hughes, and F. Shakib, “A globally convergent matrix-free algorithm for implicit time marching schemes arising in finite element analysis”, *Comp. Meth. Appl. Mech. Engng.*, **87** (1991) 281–304.
- [23] C. H. Whiting and K. E. Jansen, “A stabilized finite element method for the incompressible Navier-Stokes equations using a hierarchical basis”, *International Journal of Numerical Methods in Fluids*, (1999), SCOREC Report 9-1999.
- [24] G. Hauke and T. J. R. Hughes, “A comparative study of different sets of variables”, *Comp. Meth. Appl. Mech. Engng.*, **153** (1998) 1–44.
- [25] K. E. Jansen, “Large-eddy simulation of flow around a NACA 4412 airfoil using unstructured grids”, in *Annual Research Briefs*, Center for Turbulence Research, NASA Ames / Stanford University, (1996) 225–232.
- [26] F. Bastin, “Jet noise using large eddy simulation”, in *Annual Research Briefs*, Center for Turbulence Research, NASA Ames / Stanford University, (1996) 115–132.
- [27] F. White, *Viscous flow*. McGraw Hill, New York, 1974.
- [28] C. H. Whiting, K. E. Jansen, and S. Dey, “Hierarchical basis in stabilized finite element methods for compressible flows”, *Comp. Meth. Appl. Mech. Engng.*, (1999), SCOREC Report 11-1999.